Originally published 4 July 2013; revised 9 August 2013

www.sciencemag.org/cgi/content/full/science.1239053/DC1

Supplementary Materials for

Real-Time Dynamics of RNA Polymerase II Clustering in Live Human Cells

Ibrahim I. Cisse, Ignacio Izeddin, Sebastien Z. Causse, Lydia Boudarene, Adrien Senecal, Leila Muresan, Claire Dugast-Darzacq, Bassam Hajj, Maxime Dahan,* Xavier Darzacq*

* Corresponding author. E-mail: maxime.dahan@curie.fr (M.D.), darzacq@ens.fr (X.D.)

Published 4 July 2013 on *Science* Express
DOI: 10.1126/science.1239053

This PDF file includes

Revision 8 August 2013: The full references are listed, and the numbering for the supplementary references has been corrected. The supplementary text and the methods section have been correctly rearranged.

Supplementary Materials

Materials and Methods

Cell line engineering

Cell lines were generated from human osteosarcoma (U2OS) cells. These were grown at 37°C, in a water-saturated atmosphere containing 5% CO_2. Complete low-glucose DMEM (DMEM-C) was used as culture medium: This is composed of Dulbecco's Modified Eagle Medium (21885-025) with 1 mg/ml glucose, supplemented with 1% penicillin/streptomycin antibiotics (15140130) and 10% fetal bovine serum (FBS) South American origin (L10270106) all from **Life Technologies** (Carlsbad, CA). Cells were harvested by detaching them with Trypsin (15400-054) from **Life Technologies** (Carlsbad, CA). Transfections were carried out using *Fugene 6* (11814443001) from **Roche**, according to the supplier's recommendations.

Dendra2 cell line engineering

U2OS cells were transfected with a plasmid encoding unfused Dendra2 and kept under selection with geneticin from **Life Technologies** (10 131-027) for 2 weeks. We picked Dendra2, as it is a protein that is known not to cause artefactual clustering when fused to other proteins (*24*) and characterized as a better choice (compared with alternatives) for its single-molecule photo-stability (*25*). After harvesting, cell aggregates were discarded after a selection in a cell sieve of 40 µm and a solution of 1 million cells per milliliter of PBS was used for sorting. Low–expression level cells (500 000) were collected in a solution of PBS + 10% FBS, in tubes precoated overnight with pure FBS, before being cultured in 10-cm-diameter petri dishes.

To select the appropriate low–expression level in Dendra2-alone cell line, cells were sorted with a fluorescence-activated cell sorter (FACS ARIA III, **BD Bioscience**) with particular care of selecting not only in function of the cells relative size or granulosity (reflecting the shape and "health" of the cells), but also in function of their fluorescence level, reflecting the fluorescent protein expression level. Low fluorescent cells were selected, choosing the fluorescence level just above the fluorescence of wild-type cells.

Dendra2-Pol II and Halo-Pol II cell lines engineering

Plasmids coding for alpha-amanitin–resistant RPB1 fused to Dendra2 (Dendra2-RPB1Amr) or to Halo (Halo-RPB1Amr) were generated by replacing the yellow fluorescent protein (YFP) containing fragment in the YFP-RPB1Amr plasmid described previously (*4*) with the Dendra2-containing (or the Halo tag–containing) fragment from plasmid Dendra2C1 (home cloned) using restriction enzymes HpaI and SacII. U20S cells were grown to 70% confluence in a 6-cm petri dish and transfected either with the Dendra2-RPB1Amr or the Halo-RPB1Amr plasmids. The next day, cells were split into three 10-cm dishes, containing respectively 70%, 20%, and 10% of the cells. Selection was carried out by using 2 µg/mL alpha-amanitin (A2263) from **Sigma-Aldrich** (St. Louis, MO)**.** Upon the formation of distinct colonies, these were picked and grown separately in DMEM-C supplemented with alpha-amanitin to a concentration of 1 µg/mL. Cells were screened for expression of Dendra2-RPB1 or Halo-RPB1 by microscopic observation; the selected cell lines were further tested by Western blot.

Flavopiridol, serum-starvation, and serum-induction experiments
For flavopiridol treatment, the cells were grown in the normal culture medium before transferring to an L-15 (Leibovitz) medium from **Sigma-Aldrich** (St. Louis, MO), supplemented with 10% v/v FBS, that we used as imaging buffer for live-cell PALM acquisition. Five minutes before imaging, the L-15 imaging buffer was supplemented with 5 μM flavopiridol hydrochloride hydrate (F3055) from **Sigma-Aldrich** (St. Louis, MO).

For serum starvation and inductions, cells grown in the normal culture medium containing 10% FBS (described above in the Cell line engineering section), were transferred to serum-free medium for overnight culture at 37°C. For imaging under a serum-deprived condition, pure L-15 buffer without FBS was used. For serum-induction, the L-15 medium was supplemented with 20% FBS, 10 min before acquisition.

Fixation and antibody staining
Cells were fixed in 4% Paraformaldehyde (15714) from **Electron Microscopy Sciences** (Hatfield, PA 19440) in PBS for 10 min, permeabilized with 0.5% v/v Triton X-100 (2000-B) from **Euromedex** (Souffelweyersheim, France) in PBS with 0.5% Tween20, for 3 min and incubated in Glycine (100mM) for 10 min in PBS with 0.5% Tween20. After saturation with 3% BSA (A3059) **Sigma-Aldrich** (St. Louis, MO) in PBS with 0.5% Tween20, cells were stained by primary antibody for CTD-RPB1 (ab52202) from **Abcam** (Cambridge, UK), serine2, or serine5-phosphorylated CTD-RPB1 (clone 3E8), which were kind gifts of Dirk Eick (Hemholtz Zentrum Munich, German Research Center for Environmental Health – GmbH- Institute for Clinical Molecular Biology, Hämatologikum Marchioninistr. 25) with an overnight incubation at 4°C. As secondary antibody, Cy^{TM}5 conjugated anti-rat (ab6565) **Abcam** (Cambridge, UK) was used.

STORM specific fixation and nanobody labeling
Cells expressing YFP-fused RPB1 was prepared as described previously (*4*) and used for fixed cells 2D direct stochastic optical reconstruction microscopy (STORM) (*26,27*). The cells were plated on 35-mm round coverslips cleaned with PIRANHA solution to reduce background to the dSTORM image. Fixation with PFA protocol was then performed as indicated above. After washing with PBS, cells were permeabilized with Triton-X100 (**Sigma**- T8787) at 0.25% vol/vol in PBS for 10 min, then washed twice in PBS. An additional 30-min incubation of the cells in 4 drops of Image-iT FX (**Invitrogen** - I36933) was performed to reduce background due to unspecific binding. A blocking buffer (*PBST /1%BSA* **Sigma** A7906/*4% horse serum* **Jackson Immunoresearch** 008-000-121) was used for incubation for 45 min, followed by a 45-min incubation with 50 ng/ml anti-GFP nanobody (**Chromotek**-GFP- Trap protein ACT-CM-GFPTRAP, recognizing GFP and YFP) attached to Alexa 647; the nanobody was prepared using a protocol described previously (*28*). The cells were then washed 3 times with PBS before imaging.

Combined FISH-dSTORM sample preparation
Cell cultures were transferred into collagen (Gibco) coated culture plates and maintained in DMEM, supplemented with 10% FBS. The culture medium was removed 1 day after passage to start serum starvation, the cells were washed with PBS and fresh medium containing no FBS was added for 24h. The Halo-Pol II cells were then labeled with HaloTag TMR Ligand (Promega), following the supplier's protocol, for dSTORM imaging. The culture medium was removed and fresh medium containing 10% FBS was added for 20min before fixation.
In situ hybridization was performed as described previously (*29*). The formamide concentration was 40% in hybridization and washing mixture. The sequence of β-actin probes were the

following (1 stand for amino-allyl T):

beta actE3	A1TGTAGAAGG1GTGGTGCCAGA1TTTCTCCATG1CGTCCCAGTTGG1GA
beta actE4_1	GCC1GGATAGCAACG1ACATGGCTGGGG1GTTGAAGG1CTCAAACA1GAT
beta actE4_2	GAAG1CCAGGGCGACG1AGCACAGCT1CTCCTTAATG1CACGCACGAT1T
beta actE5	A1GTCCACGTCACAC1TCATGATGGAG1TGAAGGTAG1TTCGTGGA1GCC
beta actE6	1AACGCAACTAAGTCA1AGTCCGCC1AGAAGCATT1GCGGTGGACGA1GGA

The modified oligonucleotide probes for RNA FISH were synthesized by Eurogentec. Probes were labeled with Alexa488 (Life technology) following the protocol of the supplier. 0.5ng of each probe was used for hybridization.

Combined FISH and dSTORM Imaging

Cells were first imaged in PBS for FISH acquisition. A z-axis nanopositioner stage (Mad City Labs Inc.) was used to perform z-stacks covering the whole cell, with a distance step of 12 nm. A 488-nm laser was used to excite the FISH probes, and the luminescence of the Alexa488 dyes was collected on the CCD camera after filtering through an emission filter (Semrock FF01-525/30). After FISH acquisition, an image of the ensemble fluorescence of Pol II-Halo tag-TMR was taken using a mercury lamp as excitation source, filtered with an excitation filter (Semrock FF01-560/25), and an emission filter for the TMR fluorescence (Semrock FF01-607-36). Prior to the dSTORM acquisition, the PBS of the sample was exchanged with the reductive buffer described previously (dSTORM buffer), and the stage was positioned in the z-plane where one nascent transcription site had been observed after FISH acquisition. dSTORM acquisition was performed as described above, with 561-nm and 405-nm lasers for excitation and activation, respectively, of the TMR fluorophores.

Western blot analysis

Western blotting was optimized so as to separate the labeled mutant (Dendra2-RPB1) from unlabeled RPB1. To prevent excessive dephosphorylation of RPB1, cells were lysed by scratching in boiling SDS-loading Buffer, 1X LDS Sample Buffer (NP0007) from **Life Technologies** (Carlsbad, CA) complemented with 50 mM DTT. The total volume of buffer used for each plate was determined according to the number of cells on the plate, so as to obtain a concentration of ~5 million cells per milliliter. Volumes corresponding to equal amounts of total numbers of proteins were loaded on different lanes of a Nupage Novex 4-12% BIS-TRIS gel (NP0321BOX) from **Life Technologies** (Carlsbad, CA) migrated for 48 hours at 4°C and 80 V in a Nupage SDS MOPS Running Buffer (NP0001) from **Life Technologies** (Carlsbad, CA) then transferred to nitrocellulose membrane (10 401 396) from **GE Healthcare Life Sciences** (Piscataway, NJ) for 1 hour at 32 V, at room temperature (23°C). The membranes were stained using an antibody (Ab522002) from **Abcam** (Cambridge, UK) at dilution 1/1000, directed against the C-terminal domain of RPB1. Incubations were followed by secondary antibodies, goat anti-rabbit IgG conjugated with horseradish peroxidase (HRP) (W4011, Promega, Madison, WI). Signals were detected by ECL chemiluminescence using UptiLight HS WB Substrate (98490B-B Uptima) from **Interchim** (Montluçon France). Bands were digitized with the LAS4000 luminescence detector from **GE Healthcare Life Sciences** (Piscataway, NJ).

Image analysis and PALM reconstruction

Single-molecule detection and reconstruction of two-dimensional super-resolution images was performed as described (*30*). Raw images of single molecule signals were analyzed with an adapted version of the multiple-target tracking algorithm (MTT) (*31*). For each frame, the point-spread function (PSF) of spatially separated individual fluorophores was detected and fitted to a two-dimensional Gaussian distribution. The centre of the fit yielded the position of single molecules with nanometre accuracy (typically between 10 and 15 nm). For fixed cells we used fluorescent beads (TetraSpeck microspheres) to correct for lateral drifts during the acquisition by using a sliding window of 100 frames. Live-cell acquisitions were performed without beads so as to avoid any ambiguity or contribution from bead fluorescence in tcPALM analysis. Super-resolution images were rendered by superimposing the position coordinates of the detected single molecules, represented with a 2D Gaussian curve with the same intensity value, by using a standard deviation s that had been previously determined by the localization accuracy of single fluorophores (typically 10 nm).

For tcPALM analysis, small rectangular regions of interest (ROIs), corresponding to spatially clustered detections, are selected from "pointillist" map projecting all the detection data from individual cells as generated with the MTT algorithm. For each cluster ROI, a binary list (frame#, #_of_detections) was generated, representing each frame number and the corresponding number of detections within that given ROI for that given frame. This information was then represented in time-series (frame#, count of detection per frame) or cumulative function (frame#, total count up to frame#). This representation is the individual time-dependent cluster profile and the representation is later used for dwell time analysis.

For dwell-time analysis, bursting events were selected manually from individual clusters by defining apparent burst start and end points in the cumulative detections. We selected only the bursts of counts corresponding to more than 10 detections as we estimated that those have less than 1% probability to arise from a single molecule (Fig. S4E). For the live cell normal growth data presented in Fig. 2, for instance, on the basis of these selection criteria, we obtained, on average, 1 burst per cluster; 7% of clusters were later discarded from the analysis because their burst sizes were smaller than the selection cutoff.

Single molecule (PALM, tcPALM and dSTORM) imaging

Super-resolution PALM, tcPALM, and dSTORM image acquisitions were carried as described previously (*30*), by using an inverted Nikon Eclipse Ti microscope with a 100× oil immersion objective (N.A. 1.49). Activation and excitation lasers were combined in an external platform; the combined beam was expanded and re-collimated with a beam expander, and focused in the rear plane of the objective by using an achromatic converging lens. Images were taken in wide-field configuration. Images were acquired with an Andor iXon EMCCD camera with a pixel size of 16 μm; the image pixel size was therefore 160 nm.

Movies of 10 000 frames were acquired at a frame rate of 50 ms under continuous illumination for both, activation and imaging lasers. The z-position was maintained during acquisition by a Nikon perfect focus system (PFS); for fixed cells control samples, drifts in the x/y-plane were corrected in the post-processing of the images (as described above).

For PALM and tcPALM, laser power densities on the sample were 1.6×10^{-3} kW/cm^2 (405 nm) and 3.5 kW/cm^2 (561 nm). Single-molecule Dendra2 signals were separated with a 561 nm dichroic (Di01-R561-25636) and a single band 617 nm emission filter (FF01-617/73).

For direct STORM (dSTORM), cells were imaged in a reducing buffer composed of 50 mM MEA from **Sigma**-M6500, 30 mM glucose oxidase from **Sigma**- G6125-50Ku, 33 μg/ml catalase from **Sigma**-02071, in 10% glucose. Images were later acquired in a wide-field microscope (Nikon Ti), by shining a 640-nm laser light (**Vortran Laser technology**- 10645/B1)

onto the sample through a multiband dichroic filter (**Semrock** Di01-R405/488/561/635). The images were acquired by using an EMCCD camera (**Andor**, DU-897E-CSo-#BV). The sample was bleached with high excitation power (~3.3 kW/cm^2), where the majority of the molecules switched to the dark state, which allowed a lowered excitation power of 1 kW/cm^2 to enable a few molecules to remain blinking in the field of view. Activation laser at 488 nm (Coherent Sapphire-SAPPHIRE 488-500 CDRH) was used (~0.015kW/ cm^2) to increase the number of blinking points to achieve a constant number of activated molecules per frame (~200 detections/frame). Per cell, 30000 frames were acquired. A filter (**Semrock** FF01-676/37-25) was placed in front of the camera to detect only emission wavelength.

Supplementary Text

In order to analyse the spatial clustering of Pol II based on the detection patterns in PALM reconstruction images (Fig. S3), we adapted the pcPALM (*12*, *32*) approach that uses the pair correlation function together with two models to describe the data.

The pair correlation function $g(r)$ represents the ratio between the probability of finding two points, within the given point process, at distance r from each other and the respective probability under complete spatial randomness. In the case of complete spatial randomness, the pattern of detections are represented by a spatial Poisson process, for which the pair correlation function is $g(r) = 1$. However, because of fluorophore photophysics (for example, single-molecule stochastic blinking during image acquisition), one may expect that a single molecule produces a cluster of detection peaks owing to over-counting; in such a case the detected peaks are normally distributed N (0, σ). If the underlying spatial process describing the position of the molecules is completely random, the pair correlation function of the process associated to the location of the imaged peaks is given by (*32*)

$$g(r) = g^{\mathrm{PSF}}(r)/\rho + 1 \qquad (1)$$

with

$$g^{\mathrm{PSF}}(r) = (1/4\pi\sigma^2) \times \exp(-r^2/4\sigma^2)$$

and ρ representing the average surface density of molecules.

We consider the model in eq. 1 our null hypothesis, describing spatial randomness of the molecules' positions.

The pair correlation functions $g(r)$ for four datasets (two primary data on Pol II, in fixed and live cells, respectively, and two control data sets of Dendra2, in fixed and live cells, respectively) were computed directly from the 2D detection coordinates of a selected sub-region. The sub-region was selected such that empty spaces, including nucleolar regions, were specifically avoided. The null hypothesis model is fitted to the four datasets. Subsequently, we perform an envelope test to assess the goodness of fit, by generating independent simulations of point patterns with the parameters determined from the fit. If the empirical $g(r)$ computed from the data falls within the envelope of simulated patterns for the null hypothesis, the null hypothesis is upheld: this was the case for both Dendra2 live and fixed samples, as presented in Fig. 3, A and B, respectively. If, on the other hand, the null hypothesis is rejected, among several alternative models we choose the one proposed in the original pcPALM manuscript (*12*).

$$g(r) = g^{\mathrm{PSF}}(r)/\rho + (A \exp(-r/\xi) + 1) * g^{\mathrm{PSF}}(r), \qquad (2)$$

where * denotes the convolution operator. This model is fitted to the data in order to estimate the parameter ξ which represents the average radius of correlation for the clusters.

For the fixed Pol II data, a processing step was applied consisting of replacing molecules closer than 50 nm in successive frames with one molecule located at the averaged position of these molecules (*12*). Here, the pre-processing might be needed because in fixed cells multiple scales of clustering are observed; for the other datasets no such processing was required for the correlation $g(r)$ to be fitted to either Eq. 1 or Eq. 2. The fit of the model defined by Eq. 2 to the Pol II fixed and live cell data are plotted in Fig. S3, C and D, respectively.

The computation of point correlation functions was performed by using the R package spatstat (*33*), while the models were fitted by using the trust-region method implemented in the Curve Fitting Matlab toolbox.

The parameters σ, ρ, ξ, A for all fits are summarized in Table S1.

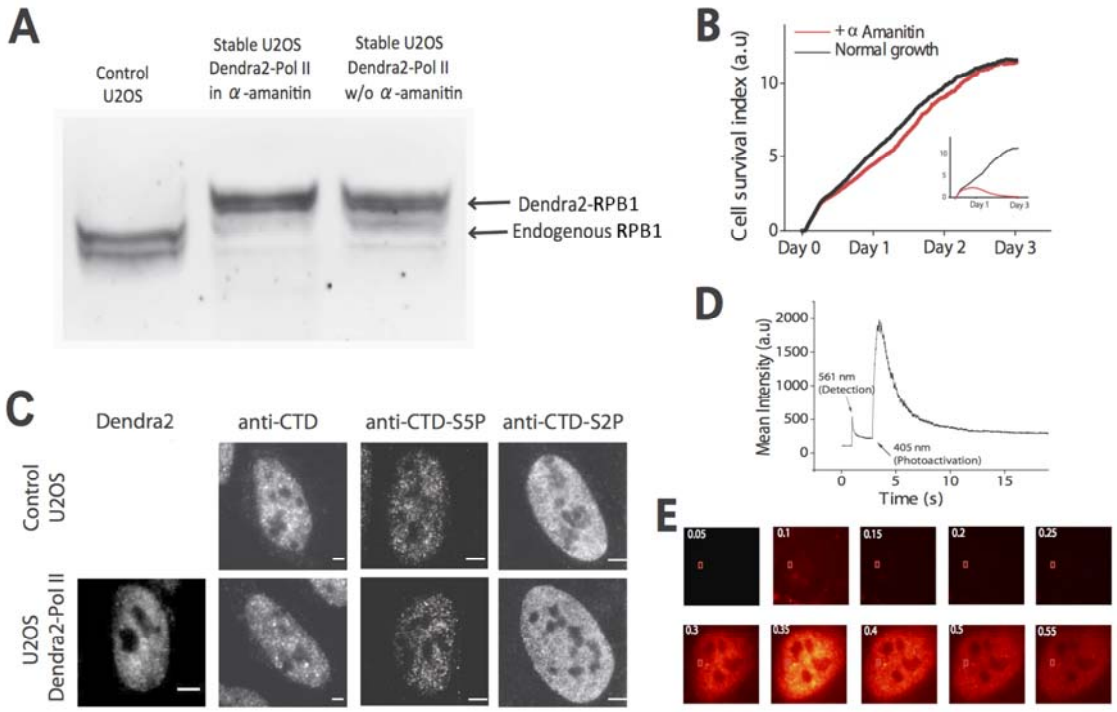

Fig. S1: New cell line enables high-resolution spatiotemporal characterization of Pol II in live cells.

(**A** and **B**) Cells are viable by replacing endogenous RPB1 with Dendra2-RPB1; Western blot separates endogenous from mutant RPB1 (A) with little evidence of endogenous RPB1 return after toxin (α-amanitin) is removed. (B) Cells survive in α-amanitin, a toxin that degrades endogenous RPB1 (B, inset) suggesting cells remain viable by functionally utilizing the mutant RPB1.

(**C**) Identical fixed cells immuno-stainings are obtained on control U2OS and our mutant U20S stably expressing Dendra2 labeled Pol II. Antibodies targeting RPB1's C-terminal domain (CTD), and phosphorylated (*7*) CTD serine5 (CTD-S5P) and serine 2(CTD-S2P) are tested. The non-homogeneous distributions of Pol II observed are consistent with previously reported non-homogeneous distributions by using comparable antibody stainings of Pol II in various cell types (*1, 4, 7, 34-37*).

(**D** and **E**) 405-nm-dependent photo-conversion is consistent with Dendra2-labeled Pol II in a living cell. Fluorescence intensity is plotted (for a small ROI in the nucleus) while the living cell is subjected to specific laser illuminations [in (D), illumination start points are indicated by arrows]; and for the same cell, a montage of the fluorescence intensity in a region centred around the nucleus, shows nuclear localization of the photo-converted dendra2 fluorescence consistent with Pol II localization (E). Time stamps in (E) are in white at the top left corners, and the red rectangle depicts the intra-nuclear region used for (D).

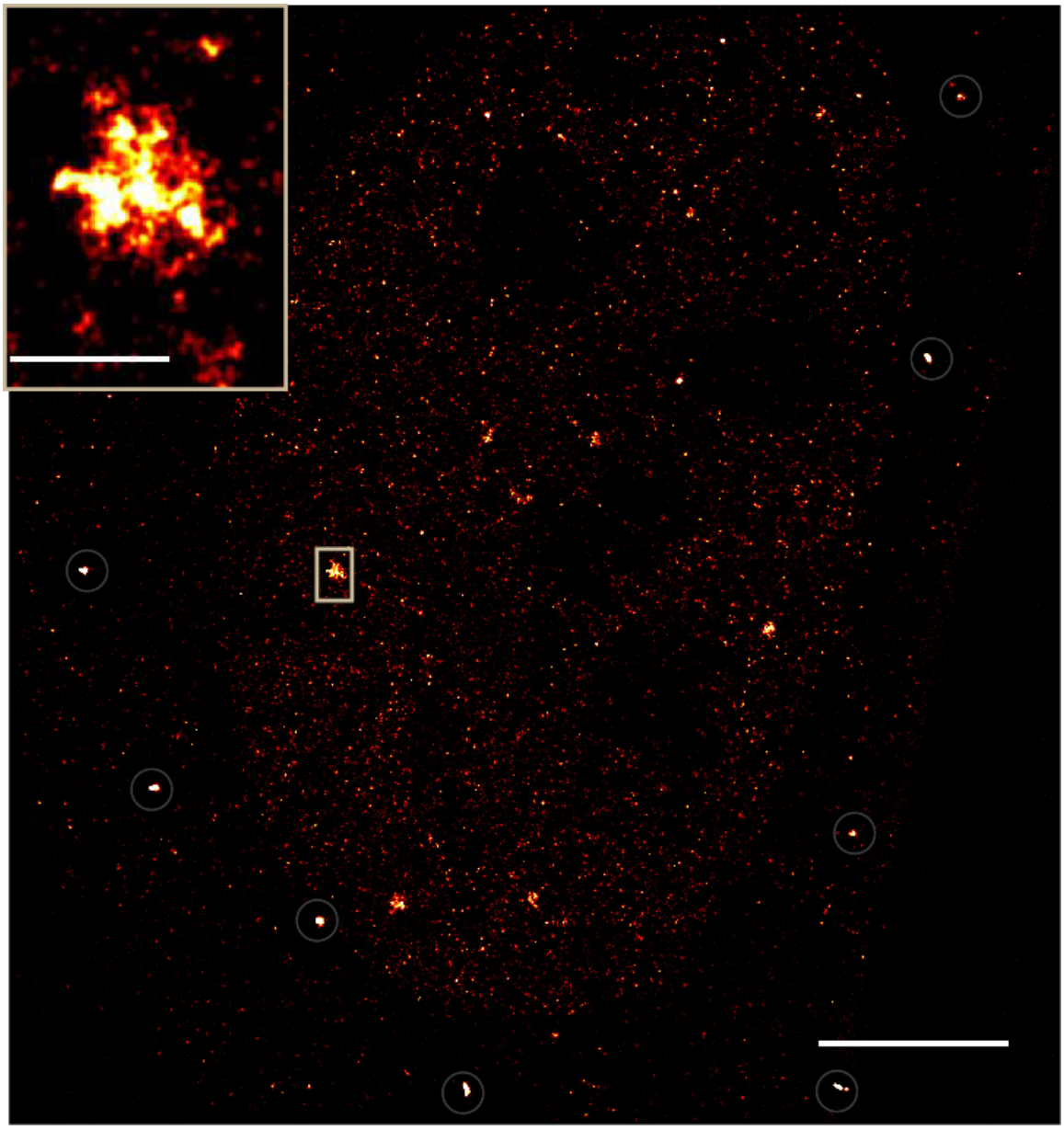

Fig. S2A. Pol II PALM super-resolution in fixed cell.

PALM super-resolution reconstruction of Dendra2-RPB1, in a region centred around the cell nucleus, shows non homogeneous distribution of Pol II; red-hot color code was used to represent the density of detections; scale bar represents 5 µm. (Inset) a zoomed-in representation of high-density (cluster) region; beads used for drift correction are denoted by gray circles; inset scale bar represents 500 nm.

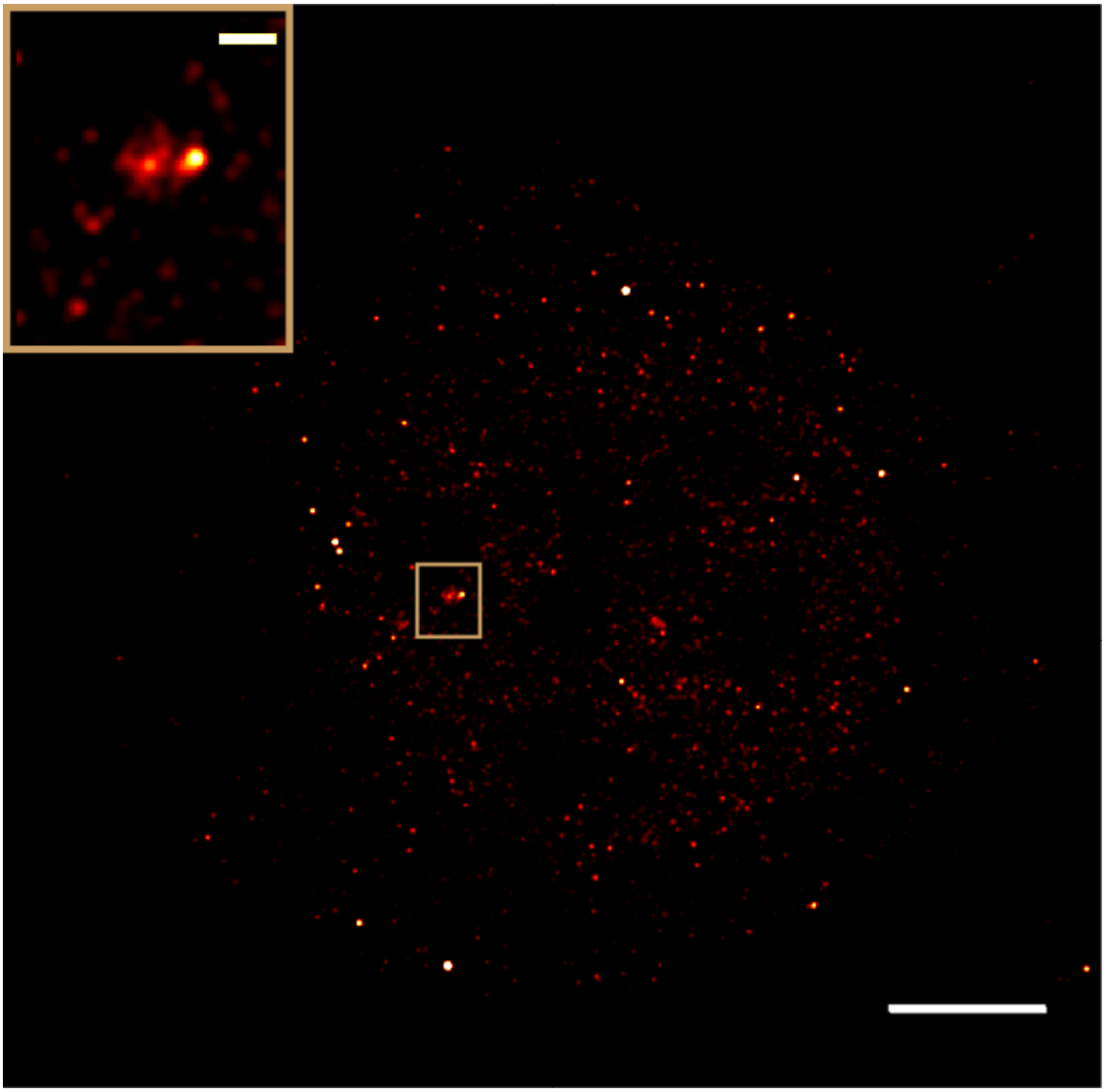

Fig. S2B. Pol II STORM super-resolution in fixed cell.

An alternative super-resolution approach to PALM, direct Stochastic Optical Reconstruction Microscopy (dSTORM) (*26, 27*), was used to image Pol II distribution in U2OS cells. As conventional antibodies against Pol II (e.g. the immunostainings in Fig. S1C) have up to 52 potential binding sites in the CTD of RPB1, which complicate cluster interpretations, we sought to investigate an approach based on a nanobody (*28*) that recognizes the yellow fluorescent protein fused to RPB1. The nanobody in turn was labelled with Alexa 647 enabling STORM imaging.

The STORM reconstructed image shows non-homogeneous distribution of Pol II in the fixed cell, in agreement with PALM imaging. In the representation above, red-hot color code was chosen to represent the density of detections and the scale bar corresponds to 5 μm. (Inset) a zoomed-in representation of a high-density region; inset scale bar represents 500 nm. However, we cannot rule out in this experiment that some YFP-RPB1 may not be accessible to the nanobody. Furthermore, fundamentally different fluorophore blinking photophysics of the Alexa 647, inherent to the STORM approach, limited us from further quantification as we had been able to do with PALM Dendra2-RPB1.

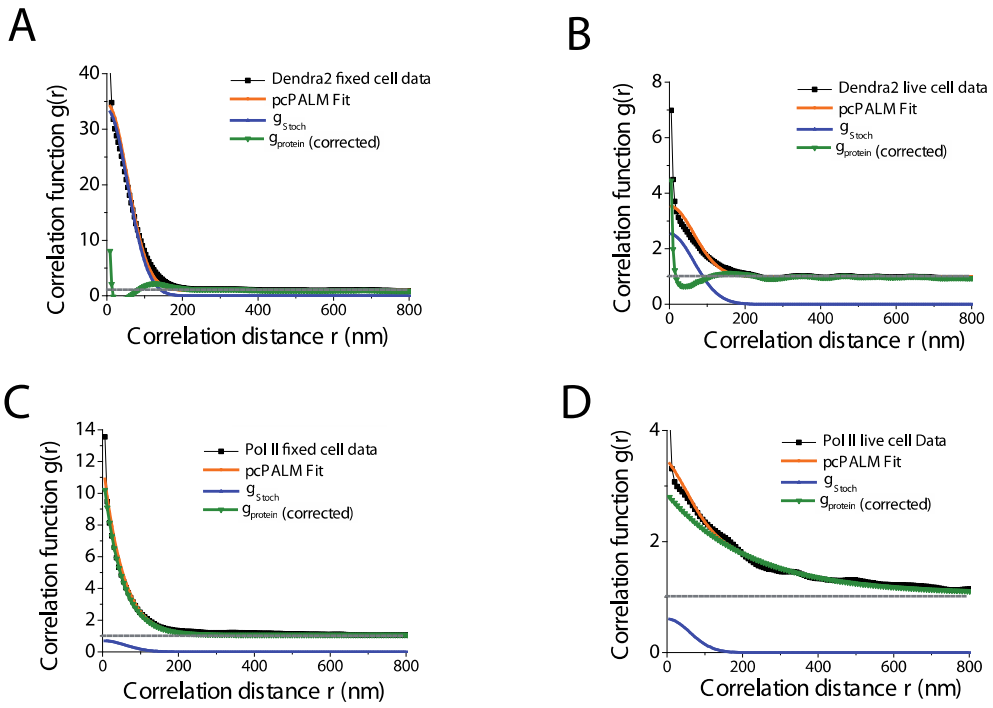

Fig. S3. Spatial clustering of Pol II distinct from single molecules revealed by pair-correlation (pcPALM) analysis.

Represented are pair correlation analyses for Dendra2 alone in fixed cell (**A**), Dendra2 alone in live cell (**B**), Dendra2-Pol II in fixed cell (**C**), and Dendra2-Pol II in live cell (**D**).

See supplementary text.

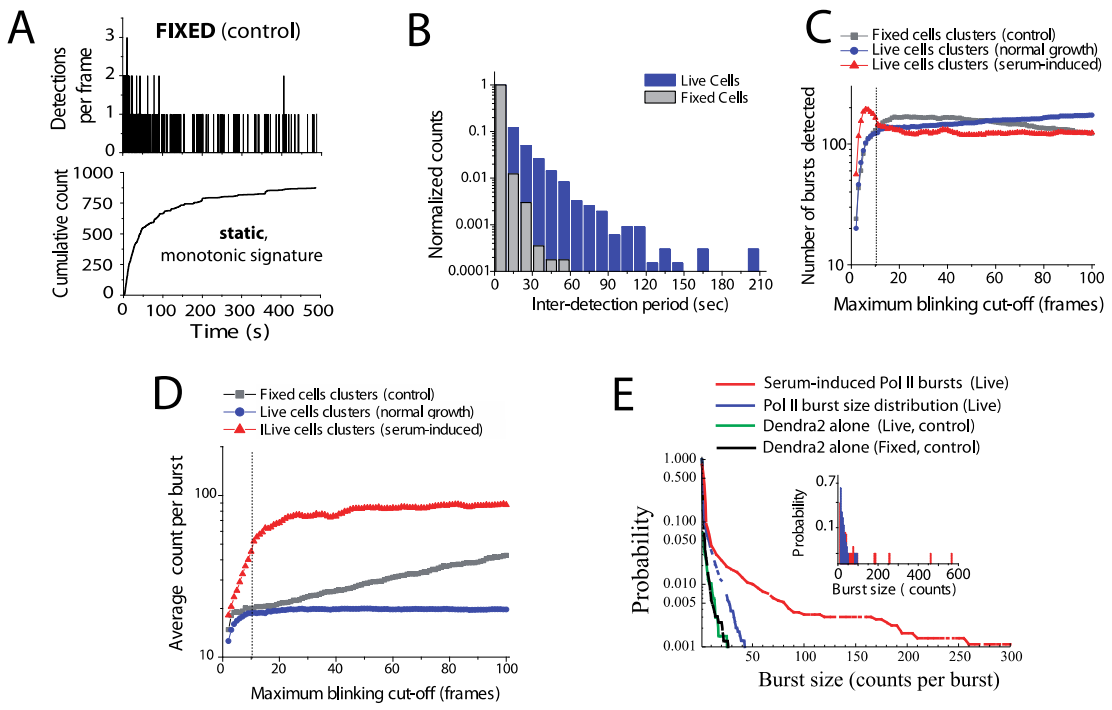

Fig. S4. Burst analyses separate live cell temporal clusters from static clusters and single-molecule stochastic detections

Samples of clusters from fixed and live cell PALM data have been selected to develop tcPALM burst analysis.

(**A**) Example of Pol II cluster profile from a fixed cell showing a gradual, monotonic cumulative-detection function which is characteristic of a static cluster stochastically activated over time followed by a gradual plateau likely representing exhaustion (photobleaching) in the pool of activated molecules.
(**B**) Live cell cluster data (as for example, in the main Fig. 2, A-D) has significantly longer dark times (periods separating frames with a detected particle) compared to fixed cell clusters. Significantly larger dark times in live cells, compared to fixed cells under identical condition, are consistent with polymerases that are highly transient, and did not stay static for a full saturated detections. A larger inter-detections period suggests a burst separation based on a "cutoff dark time" may be possible, i.e. an analysis based on a maximum number of dark frames allowed for consecutive detections in a time-series to be considered as part of the same burst.
(**C**) The dark times observed (for example in Fig **S4B**) may be in part be due single-molecule fluorophore photophysics (blinking or intensity fluctuations); such events would significantly affect the number of bursts detected in an automated burst selection depending on the cutoff parameter chosen. Therefore we sought to find if there was an optimal cutoff range for which the inherent kinetics (at least in live cells and serum induced live cell data) would not be affected significantly (i.e. a plateau in this representation). To find an optimal cutoff, we performed automated tests on fixed and live cell PALM cluster data, and calculated the average number of burst detected per cutoff parameter. As it is a region relative invariance (i.e. a plateau in the readout, and not the exact amplitude) which was of interest to us in this graph [and in (S4D)] we sampled different numbers of clusters to

overlap the curves for better visualization: for 104 Pol II clusters in live cells, we overlapped 88 Pol II in serum induced clusters and only 20 Pol II clusters from fixed cells because there were significantly more detection counts per clusters in fixed compared to live cells as could be evidenced by comparing the examples in Fig. S4A and Fig. 2, A-D. We were satisfied with a cutoff of 10 dark frames because drastic fluctuations in the readout (here the number of bursts detected per cluster) stabilized on all samples by 10 dark frames cutoff (vertical dashed line).

(**D**) To test further the original hypothesis that a cutoff based detection can uniquely separate bursts in live cells independently of the cutoff parameter, we computed the average count per busrt detected in sampled data sets as a function of cutoff (here only bursts of at least 10 detection counts were included for single molecule arguments explained in the next part S4E). We observe that the live cell clusters indeed reached a plateau suggesting the average size of detected bursts was independent of the cutoff parameter. This plateau was sustained up to one order of magnitude beyond our selected blinking cutoff of 10 frames. The fixed cell data on the other hand remained highly sensitive to the cutoff, with a steep increase suggesting that as longer dark time is allowed within a burst, one would continuously associate different stochastic detections into a single burst without the ability to uniquely separate detections in fixed cells, as data from live cells would allow. These results suggest that a cutoff based burst analysis is suitable for our live cell data, but a burst analysis does not make sense for the fixed data of completely static Pol II clusters.

(**E**) Burst detection analysis reveals temporally clustered Pol II in live cell (blue) and serum induction (red) have statistically larger detection counts than single Dendra2 fluorophores (black and green). To investigate the distribution of bursts counts from individual Dendra2 fluorophores, we engineered a cell line expressing the fluorophore alone not fused to any other protein (see Methods section). We acquired data in both live and fixed cells and obtained localization points in both experiments. Under identical detection settings, the rank order distributions of the burst sizes detected from the individual fluorophores (equivalent to: 1- P_{cumul} where P_{cumul} is the cumulative probability distribution of all detected burst sizes) is compared to the Pol II live cell burst data. We see a clear dissimilarity between Pol II and Dendra2 distributions, suggesting that Pol II temporal clusters are clearly distinct from any possible fluorophore photophysics. We note that based on the distribution of the Dendra2 bursts, there is less than 0.001 probability (0.1%) for the bursts of more than 20 counts (such as those observed for live cells in the main Fig. 2, A-C) to come from any unusually long lived single-molecule detection. From this data, we observe that imposing a selection criteria based on the burst size would allow us to minimize the chance of miss-assignment of cluster from single molecule detections; however since live cell clusters are transient we might miss some short lived clusters. We found 10 counts to be a suitable minimum burst size as it represents a probability of less than 1% of coming from a single molecule. This means however that we may not be analysing a number of short lived Pol II clusters which do not stay assembled long enough for accumulating more than 10 counts under our PALM data acquisition settings.

(Inset) Histograms of the probability distribution comparing Pol II cluster sizes under serum induction and normal growth are presented. These distributions show a drastic increase in the higher detection counts of burst, suggesting that serum-induction has significantly increased Pol II cluster bursts, consistent with what is observed by comparing the cumulative counts in the detection profiles represented in Fig. 2 and Fig. 3 of the main manuscript.

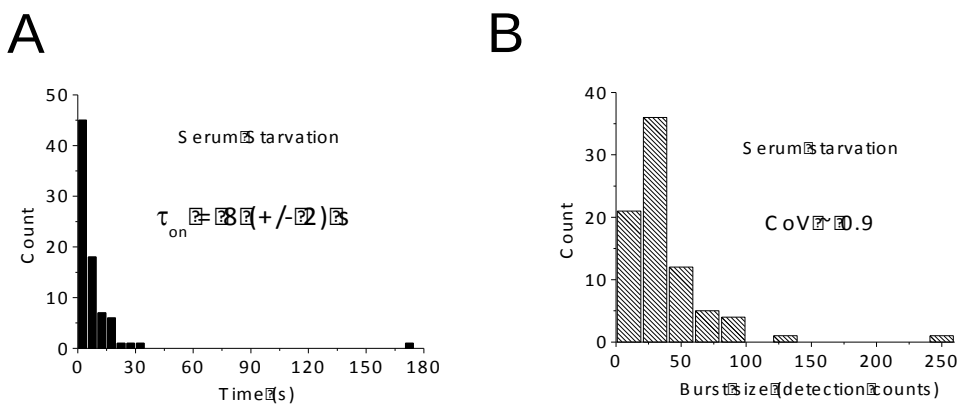

Fig. S5. Serum-deprived Pol II clustering kinetics.

(A) The distribution of cluster lifetimes from serum-starved cells is presented. The average dwell time obtained was 8 (± 2) s, more comparable to normal growth [5.1 s] than serum induced [49s] cells. (**B)** The distribution of burst sizes yield an average of 37 (± 4) counts, with bursts rarely spanning above ~100 detection counts, more comparable with normal cell bursts (main Fig. 3D, blue/inset) than serum induced bursts (main Fig. 3D, red); CoV denotes the coefficient of variation obtained for the distribution. Here, 77 Pol II cluster loci were obtained and analysed from 4 cells that were serum-deprived overnight and imaged in serum-free medium. Overall these results suggest that the orders of magnitude changes in clustering dynamics observed with serum addition (main Fig. 3) are attributable to serum-induction only changes in cell state, and not serum-deprivation.

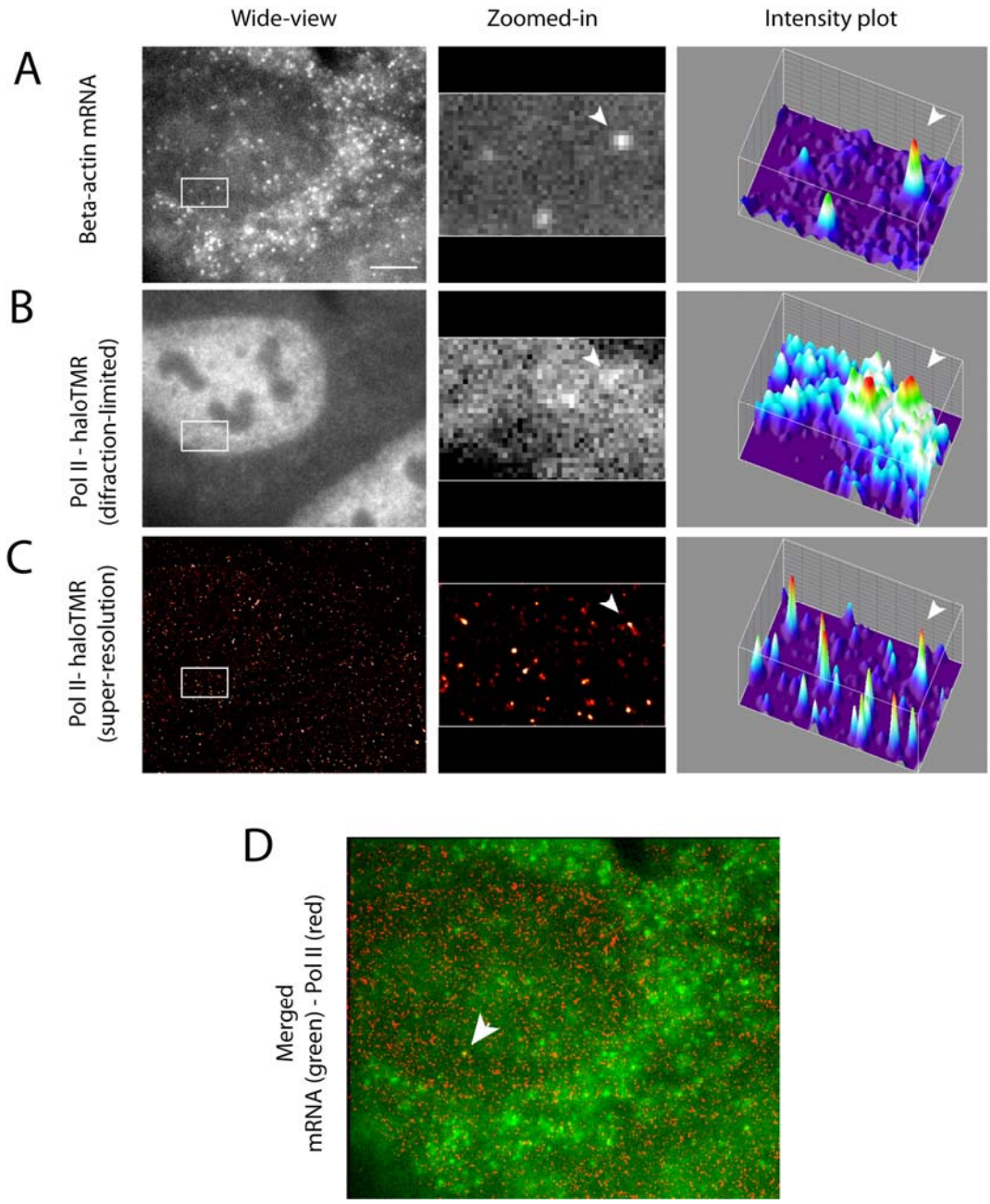

Fig. S6: Fluorescence *in situ* hybridization (FISH) nascent RNA visualization of serum-induced Beta-actin gene locus.

(A) Upon serum-induction, site of nascent transcription of endogenous beta-actin gene can be observed in fixed cells by using FISH (*38, 39*) (**B)** Diffraction-limited fluorescence imaging shows Pol II enrichment around transcription site (**C)** Super-resolution (direct STORM) (*40*) imaging of Pol II in the vicinity of transcription site. (**D)** Merged image of beta-actin mRNA and Pol II STORM localizations. Arrows indicate nascent mRNA beta-actin transcription site as determined by FISH. We note here that due to different imaging conditions between FISH and STORM, and given the protein-denaturing nature of FISH labeling in fixed cells, we could not find an optimal condition for all imaging. Nevertheless,

these results demonstrate Pol II accumulation at the transcription site of an active serum-induced gene.

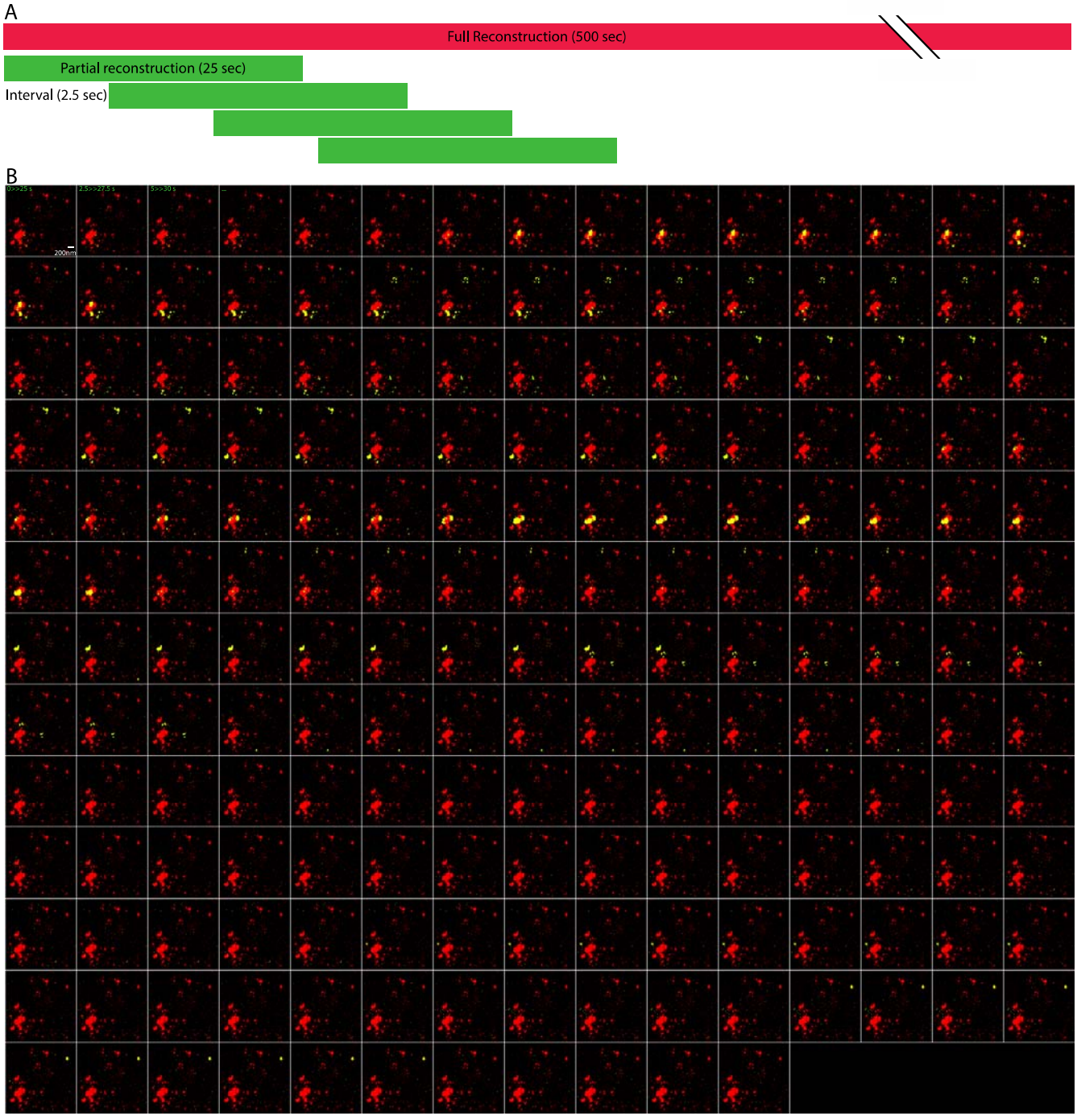

Fig. S7: Sliding-window illustration of the spatial distribution of Pol II bursting events within a cluster locus.

(A) Scheme of the sliding-window parameters (not to scale). A full projection, representing every detection for all 10000 frames (500 s), is represented in red (top). A sample window representing the projection of only detections within 500 adjacent frames (25 s) is computed from the first frame, and tiled for the equivalent window (same size) every 2.5 s afterwards. **(B)** Images representing the full projection coordinates (in red) and the respective window coordinate (in green). Aggregates of detections do not seem to diffuse but rather appear and

disappear in temporally distinct bursts even as their loci are adjacent and may appear as one larger aggregate when projected on the total background. We add a cautionary note that a sliding window analysis on PALM is not the same information as the real-time spatiotemporal distribution. While this can give powerful insights on any evidence from slow drifts or diffusions (*41*), it could also be particularly misleading for interpreting transient dynamics . For example in the pictures above individual bursting events seemingly staying on for 10 consecutive frames could very well have appeared or disappeared within a few frames [note that 10frames = window size (25s)/ step size (2.5s)] which tcPALM reveals.

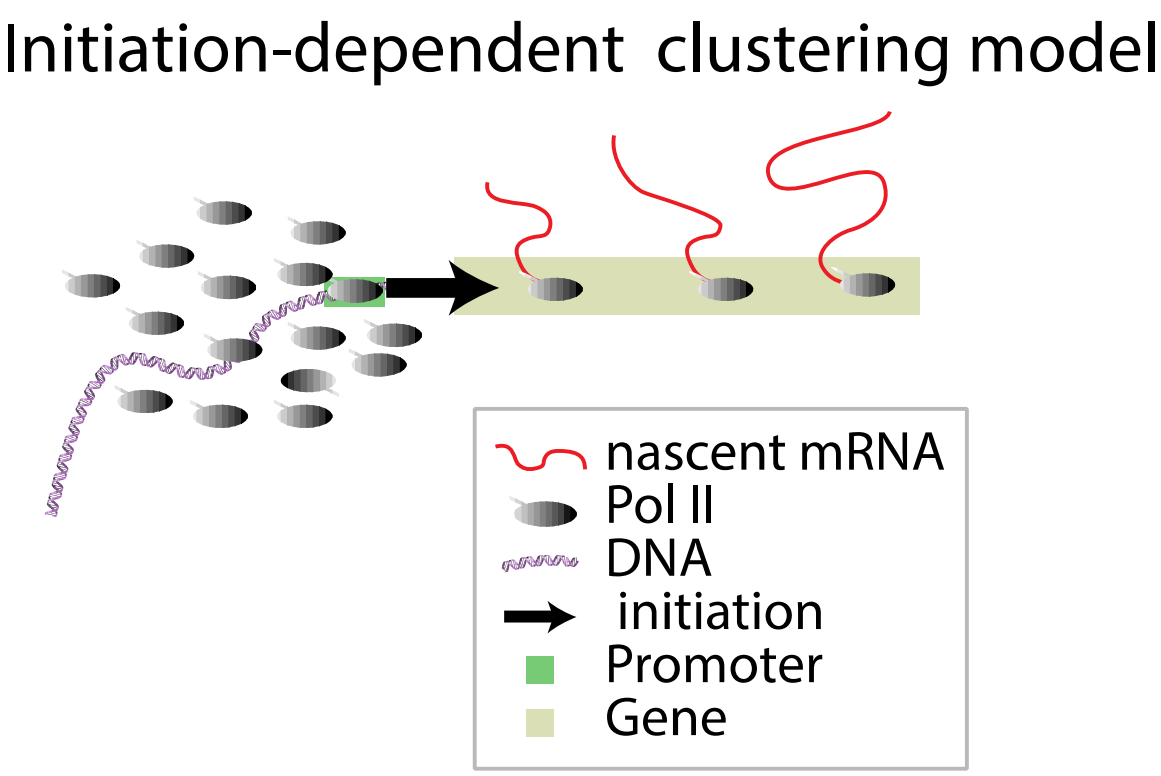

Fig. S8: Initiation-dependent clustering model.

Model whereby local crowding of Pol II may help in the initiation steps of transcription but clusters need not stay assembled throughout elongation.

Table S1. Parameters estimated from the best-fitting model to the data. σ and ξ are given in nanometer, A in counts, and ρ in counts per pixel (of 160 nm). Errors represent standard error on the fitted value.

Data	Best fit model	σ (nm)	ρ	ξ (nm)	A
Dendra fixed	Eq.1	42 ± 2	0.03	-	-
Dendra live	Eq.1	45 ± 2	0.38	-	-
Pol II fixed	Eq.2	41 ± 1	0.01	94 ± 5	1.7
Pol II live	Eq.2	43 ± 1	0.54	220 ± 17	1.6

References and Notes

1. P. R. Cook, The organization of replication and transcription. *Science* **284**, 1790–1795 (1999). doi:10.1126/science.284.5421.1790 Medline

2. P. Fraser, W. Bickmore, Nuclear organization of the genome and the potential for gene regulation. *Nature* **447**, 413–417 (2007). doi:10.1038/nature05916 Medline

3. T. Misteli, Beyond the sequence: Cellular organization of genome function. *Cell* **128**, 787–800 (2007). doi:10.1016/j.cell.2007.01.028 Medline

4. X. Darzacq, Y. Shav-Tal, V. de Turris, Y. Brody, S. M. Shenoy, R. D. Phair, R. H. Singer, In vivo dynamics of RNA polymerase II transcription. *Nat. Struct. Mol. Biol.* **14**, 796–806 (2007). doi:10.1038/nsmb1280 Medline

5. J. Yao, K. M. Munson, W. W. Webb, J. T. Lis, Dynamics of heat shock factor association with native gene loci in living cells. *Nature* **442**, 1050–1053 (2006). doi:10.1038/nature05025 Medline

6. H. Kimura, K. Sugaya, P. R. Cook, The transcription cycle of RNA polymerase II in living cells. *J. Cell Biol.* **159**, 777–782 (2002). doi:10.1083/jcb.200206019 Medline

7. H. Sutherland, W. A. Bickmore, Transcription factories: Gene expression in unions? *Nat. Rev. Genet.* **10**, 457–466 (2009). doi:10.1038/nrg2592 Medline

8. M. Becker, C. Baumann, S. John, D. A. Walker, M. Vigneron, J. G. McNally, G. L. Hager, Dynamic behavior of transcription factors on a natural promoter in living cells. *EMBO Rep.* **3**, 1188–1194 (2002). doi:10.1093/embo-reports/kvf244 Medline

9. K. Sugaya, M. Vigneron, P. R. Cook, Mammalian cell lines expressing functional RNA polymerase II tagged with the green fluorescent protein. *J. Cell Sci.* **113**, 2679–2683 (2000). Medline

10. E. Betzig, G. H. Patterson, R. Sougrat, O. W. Lindwasser, S. Olenych, J. S. Bonifacino, M. W. Davidson, J. Lippincott-Schwartz, H. F. Hess, Imaging intracellular fluorescent proteins at nanometer resolution. *Science* **313**, 1642–1645 (2006). doi:10.1126/science.1127344 Medline

11. S. T. Hess, T. P. K. Girirajan, M. D. Mason, Ultra-high resolution imaging by fluorescence photoactivation localization microscopy. *Biophys. J.* **91**, 4258–4272 (2006). doi:10.1529/biophysj.106.091116 Medline

12. P. Sengupta, T. Jovanovic-Talisman, D. Skoko, M. Renz, S. L. Veatch, J. Lippincott-Schwartz, Probing protein heterogeneity in the plasma membrane using PALM and pair correlation analysis. *Nat. Methods* **8**, 969–975 (2011). doi:10.1038/nmeth.1704 Medline

13. We note that, in live-cell PALM experiments, only a fraction of the molecules present can be localized; highly mobile or nonphotoactive molecules may be present but not detected. Therefore, tcPALM is not a measure of the total number of molecules present but rather an indication of the relative fluctuations of fluorescent molecules transiently present at a given locus.

14. R. E. Herrera, P. E. Shaw, A. Nordheim, Occupation of the c-fos serum response element in vivo by a multi-protein complex is unaltered by growth factor induction. *Nature* **340**, 68–70 (1989). doi:10.1038/340068a0 Medline

15. N. Mackman, B. J. Fowler, T. S. Edgington, J. H. Morrissey, Functional analysis of the human tissue factor promoter and induction by serum. *Proc. Natl. Acad. Sci. U.S.A.* **87**, 2254–2258 (1990). doi:10.1073/pnas.87.6.2254 Medline

16. H. R. Herschman, Primary response genes induced by growth factors and tumor promoters. *Annu. Rev. Biochem.* **60**, 281–319 (1991). doi:10.1146/annurev.bi.60.070191.001433 Medline

17. V. M. Weake, J. L. Workman, Inducible gene expression: Diverse regulatory mechanisms. *Nat. Rev. Genet.* **11**, 426–437 (2010). doi:10.1038/nrg2781 Medline

18. Z. Ni, A. Saunders, N. J. Fuda, J. Yao, J. R. Suarez, W. W. Webb, J. T. Lis, P-TEFb is critical for the maturation of RNA polymerase II into productive elongation in vivo. *Mol. Cell. Biol.* **28**, 1161–1170 (2008). doi:10.1128/MCB.01859-07 Medline

19. O. Bensaude, Inhibiting eukaryotic transcription: Which compound to choose? How to evaluate its activity? *Transcription* **2**, 103–108 (2011). doi:10.4161/trns.2.3.16172 Medline

20. P. B. Rahl, C. Y. Lin, A. C. Seila, R. A. Flynn, S. McCuine, C. B. Burge, P. A. Sharp, R. A. Young, c-Myc regulates transcriptional pause release. *Cell* **141**, 432–445 (2010). doi:10.1016/j.cell.2010.03.030 Medline

21. S.-H. Chao, K. Fujinaga, J. E. Marion, R. Taube, E. A. Sausville, A. M. Senderowicz, B. M. Peterlin, D. H. Price, Flavopiridol inhibits P-TEFb and blocks HIV-1 replication. *J. Biol. Chem.* **275**, 28345–28348 (2000). doi:10.1074/jbc.C000446200 Medline

22. N. J. Fuda, M. B. Ardehali, J. T. Lis, Defining mechanisms that regulate RNA polymerase II transcription in vivo. *Nature* **461**, 186–192 (2009). doi:10.1038/nature08449 Medline

23. D. R. Larson, D. Zenklusen, B. Wu, J. A. Chao, R. H. Singer, Real-time observation of transcription initiation and elongation on an endogenous yeast gene. *Science* **332**, 475–478 (2011). doi:10.1126/science.1202142 Medline

24. D. Landgraf, B. Okumus, P. Chien, T. A. Baker, J. Paulsson, Segregation of molecules at cell division reveals native protein localization. *Nat. Methods* **9**, 480–482 (2012). doi:10.1038/nmeth.1955 Medline

25. S.-H. Lee, J. Y. Shin, A. Lee, C. Bustamante, Counting single photoactivatable fluorescent molecules by photoactivated localization microscopy (PALM). *Proc. Natl. Acad. Sci. U.S.A.* **109**, 17436–17441 (2012). doi:10.1073/pnas.1215175109 Medline

26. M. Heilemann, S. van de Linde, M. Schüttpelz, R. Kasper, B. Seefeldt, A. Mukherjee, P. Tinnefeld, M. Sauer, Subdiffraction-resolution fluorescence imaging with conventional fluorescent probes. *Angew. Chem. Int. Ed.* **47**, 6172–6176 (2008). doi:10.1002/anie.200802376 Medline

27. M. J. Rust, M. Bates, X. Zhuang, Sub-diffraction-limit imaging by stochastic optical reconstruction microscopy (STORM). *Nat. Methods* **3**, 793–796 (2006). doi:10.1038/nmeth929 Medline

28. J. Ries, C. Kaplan, E. Platonova, H. Eghlidi, H. Ewers, A simple, versatile method for GFP-based super-resolution microscopy via nanobodies. *Nat. Methods* **9**, 582–584 (2012). doi:10.1038/nmeth.1991 Medline

29. D. Fusco, N. Accornero, B. Lavoie, S. M. Shenoy, J. M. Blanchard, R. H. Singer, E. Bertrand, Single mRNA molecules demonstrate probabilistic movement in living mammalian cells. *Curr. Biol.* **13**, 161–167 (2003). doi:10.1016/S0960-9822(02)01436-7 Medline

30. I. Izeddin, C. G. Specht, M. Lelek, X. Darzacq, A. Triller, C. Zimmer, M. Dahan, Super-resolution dynamic imaging of dendritic spines using a low-affinity photoconvertible actin probe. *PLoS ONE* **6**, e15611 (2011). doi:10.1371/journal.pone.0015611 Medline

31. A. Sergé, N. Bertaux, H. Rigneault, D. Marguet, Dynamic multiple-target tracing to probe spatiotemporal cartography of cell membranes. *Nat. Methods* **5**, 687–694 (2008). doi:10.1038/nmeth.1233 Medline

32. S. L. Veatch, B. B. Machta, S. A. Shelby, E. N. Chiang, D. A. Holowka, B. A. Baird, Correlation functions quantify super-resolution images and estimate apparent clustering due to over-counting. *PLoS ONE* **7**, e31457 (2012). doi:10.1371/journal.pone.0031457 Medline

33. A. Baddeley, R. Turner, Spatstat: An R package for analyzing spatial point patterns. *J. Stat. Softw.* **12**(6), 1 (2005).

34. C. S. Osborne, L. Chakalova, K. E. Brown, D. Carter, A. Horton, E. Debrand, B. Goyenechea, J. A. Mitchell, S. Lopes, W. Reik, P. Fraser, Active genes dynamically colocalize to shared sites of ongoing transcription. *Nat. Genet.* **36**, 1065–1071 (2004). doi:10.1038/ng1423 Medline

35. C. Morey, C. Kress, W. A. Bickmore, Lack of bystander activation shows that localization exterior to chromosome territories is not sufficient to up-regulate gene expression. *Genome Res.* **19**, 1184–1194 (2009). doi:10.1101/gr.089045.108 Medline

36. F. J. Iborra, A. Pombo, D. A. Jackson, P. R. Cook, Active RNA polymerases are localized within discrete transcription "factories' in human nuclei. *J. Cell Sci.* **109**, 1427–1436 (1996). Medline

37. J. M. Brown, J. Green, R. P. das Neves, H. A. Wallace, A. J. Smith, J. Hughes, N. Gray, S. Taylor, W. G. Wood, D. R. Higgs, F. J. Iborra, V. J. Buckle, Association between active genes occurs at nuclear speckles and is modulated by chromatin environment. *J. Cell Biol.* **182**, 1083–1097 (2008). doi:10.1083/jcb.200803174 Medline

38. A. M. Femino, F. S. Fay, K. Fogarty, R. H. Singer, Visualization of single RNA transcripts in situ. *Science* **280**, 585–590 (1998). doi:10.1126/science.280.5363.585 Medline

39. T. e. Lionnet, K. Czaplinski, X. Darzacq, Y. Shav-Tal, A. L. Wells, J. A. Chao, H. Y. Park, V. de Turris, M. Lopez-Jones, R. H. Singer, A transgenic mouse for in vivo detection of endogenous labeled mRNA. *Nat. Methods* **8**, 165–170 (2011). doi:10.1038/nmeth.1551 Medline

40. S. van de Linde, A. Löschberger, T. Klein, M. Heidbreder, S. Wolter, M. Heilemann, M. Sauer, Direct stochastic optical reconstruction microscopy with standard fluorescent probes. *Nat. Protoc.* **6**, 991–1009 (2011). doi:10.1038/nprot.2011.336 Medline

41. R. Wombacher, M. Heidbreder, S. van de Linde, M. P. Sheetz, M. Heilemann, V. W. Cornish, M. Sauer, Live-cell super-resolution imaging with trimethoprim conjugates. *Nat. Methods* **7**, 717–719 (2010). doi:10.1038/nmeth.1489 Medline